

# Precipitation and Growth of MnS Inclusions in Non-quenched and Tempered Steel Under the Influence of Solute Micro-segregations During Solidification



JUNYU LIU, CHENGSONG LIU, RUIJUAN BAI, WEI WANG, QINGBO WANG, HUA ZHANG, and HONGWEI NI

Precipitation and growth behaviors of MnS inclusions during the solidification of non-quenched and tempered steel have been experimentally and thermodynamically investigated. Effects of cooling method and cooling rate on the morphologies, size distributions, number densities, and average diameters of MnS inclusions in steels were systematically revealed. Coupled with thermodynamic calculation of MnS precipitation, two solute element micro-segregation models, Clyne–Kurz model and Ohnaka model, were introduced and improved by taking the micro-segregations of silicon, oxygen, and other solute elements into account during the steel solidification. The MnS inclusion growth was estimated according to the model calculation results. A non-linear fitting curve equation for describing the relationship between cooling rate of molten steel  $v$  and average inclusion diameter  $d$  was acquired by experiments:  $d = 10.726v^{-0.438}$ . At the cooling rate of  $R_c = 1.26 \text{ K s}^{-1}$ , the solidification fraction values for MnS precipitation in the two models were 0.929 and 0.931, respectively. Precipitation and growth of the MnS inclusions during solidification were well predicted by the improved Clyne–Kurz and Ohnaka solute element micro-segregation models by comparison of experimental and calculated results. Both the two models were validated and could be judged as equal in this work.

<https://doi.org/10.1007/s11663-023-02718-3>

© The Minerals, Metals & Materials Society and ASM International 2023

## I. INTRODUCTION

TO save energy and reduce production cost, non-quenched and tempered steel is developed through the addition of alloy elements Nb, Ti, V, and N into structural carbon steels and alloy steels. Those elements would precipitate as carbides or nitrides which contribute to grain refining and precipitation strengthening of the steel.<sup>[1,2]</sup> Thus, although the whole heating, quenching and tempering treatment processes after

forging are omitted, with reasonable cooling control methods, the steels still have excellent mechanical properties including high strength, plasticity, and fatigue resistance, *etc.*, which are close to or even higher than those of the quenched and tempered steels. Nowadays, non-quenched and tempered steels are commonly applied in the green manufacturing processes of mechanical parts such as gears, shafts and rods.

Sulfur element is commonly added into non-quenched and tempered steel to produce free-cutting steels. On account of the micro-segregations of solute Mn and S elements in the steel, MnS phase generally precipitates either as standalone pure MnS inclusions or as a part of complex sulfide-oxide inclusions in mushy region during solidification. With the decrease of temperature to a certain value, the interdendritic enrichment of those solute elements is exacerbated. The actual activity products of MnS inclusion are prone to be higher than their equilibrium ones which lead to the precipitation and growth of MnS inclusions. Actually, a typical MnS inclusion indeed has good plasticity at high temperature and is really deformable during hot rolling. Although those MnS phases play a role as lubricant in free-cutting steel to lower frictional resistance and promote machinability during mechanical machining, excessive elongation of them after hot rolling, especially those large ones, would lead to the mechanical anisotropy of steel, impair the

---

JUNYU LIU, CHENGSONG LIU, HUA ZHANG and HONGWEI NI are with the The State Key Laboratory of Refractories and Metallurgy, Wuhan University of Science and Technology, Wuhan 430081, P.R. China and also with the Hubei Provincial Key Laboratory for New Processes of Ironmaking and Steelmaking, Wuhan University of Science and Technology, Wuhan 430081, P.R. China. Contact e-mail: liuchengsong@wust.edu.cn; nihongwei@wust.edu.cn RUIJUAN BAI and QINGBO WANG are with the The State Key Laboratory of Refractories and Metallurgy, Wuhan University of Science and Technology and also with the Henan Jiyuan Iron & Steel (Group) Co., Ltd, Jiyuan 459000, P.R. China. WEI WANG is with the Henan Jiyuan Iron & Steel (Group) Co., Ltd.

Manuscript submitted October 15, 2022; accepted December 28, 2022.

Article published online January 20, 2023.

mechanical properties and ultimately result in the degradation of steel product quality and service performance.<sup>[3–7]</sup> Precise control of MnS inclusion characteristics during solidification is of great importance for the production of the non-quenched and tempered steel with high-quality.

To better understand precipitation and growth behaviors of MnS phases during solidification of molten steel, a series of studies have been conducted.<sup>[8–12]</sup> Diederichs *et al.*<sup>[13]</sup> proposed a model to describe the solidification of a medium carbon steel grade, the micro-segregations of manganese and sulfur and the subsequent precipitation of MnS. An approach for predicting MnS size as a function of the Mn and S contents was presented. Xie *et al.*<sup>[14]</sup> studied the effects of solute elements on the formation of MnS in the micro-alloyed non-tempered steel. A novel coupling model of micro-segregation and MnS precipitation during solidification using the finite-difference method was built to determine the precipitation temperature of MnS. Shu *et al.*<sup>[15]</sup> developed a model coupled with Kampmann–Wagner element micro-segregation model to evaluate MnS inclusion precipitation kinetics during steel solidification. Relationships among cooling rate, S concentration and MnS precipitation behavior have been revealed by model calculations. In those studies, to quantify the enrichment of Mn and S during solidification, the mechanisms of MnS precipitation and growth were analyzed by some solute micro-segregation models. However, the effects of micro-segregation of other solute elements such as silicon, phosphorus, oxygen and nitrogen on the thermodynamics and kinetics of MnS inclusion precipitation and growth behaviors were scarcely taken into consideration. Actually, the changes in those element concentrations during solidification due to micro-segregation would also affect the activity coefficients of Mn and S, the solidus and liquidus temperatures of steel, and some other thermodynamics and kinetics data. As the steel solidification proceeds, these influences would accumulate and become non-negligible on the precipitation and growth behaviors of MnS phases. In addition, the cooling rate varies greatly in the cross section of the continuous casting slab where the surface temperature generally declines much faster than the center temperature. Longer solidification time and lower cooling rate would result in relatively larger MnS inclusions and aggravate the mechanical anisotropy of steel after hot rolling process. Improvement of such solute element micro-segregation models to provide more accurate prediction on the precipitation and growth behaviors of MnS inclusions in the continuous casting slab has crucial practical and theoretic significances.

In this paper, the characteristic variations of MnS inclusions in non-quenched and tempered steel after cooling experiments were studied. Influences of cooling method and cooling rate on the morphologies, size distributions, number densities, and average diameters of MnS inclusions in steels were systematically revealed. Coupled with thermodynamic calculation of MnS precipitation, two solute element micro-segregation models, Clyne–Kurz and Ohnaka

models,<sup>[16,17]</sup> were introduced and improved by taking the micro-segregations of silicon, oxygen, and other solute elements into account during the steel solidification. Relationships among cooling method, cooling rate, and MnS inclusion size were predicted and compared with the experimental results to verify the validity of those models.

## II. EXPERIMENTAL METHODS

### A. Steel Solidification Experiments

Table I shows the chemical composition of the non-quenched and tempered steel which is continuously cast into a 240 mm × 240 mm billet in a steel plant and employed as experimental raw material. Solidification experiments of the steel were conducted in a high temperature resistance furnace under an Ar gas atmosphere (purity: 99.9 pct). 300 g steel was heated in an alumina crucible (inner diameter: 60 mm, height: 100 mm) at 1873 K (1600 °C) for 30 minutes to reach full melting and good homogeneity. Figure 1(a) represents the schematic diagram of the experimental apparatus. A platinum–rhodium thermocouple was employed to monitor the furnace heating temperature. The temperature increase rate before isothermal heating at 1873 K (1600 °C) was 5 K min<sup>-1</sup>. After the holding period at 1873 K (1600 °C), the molten steel was conducted with four different cooling approaches, including furnace cooling, air cooling, water cooling, and liquid nitrogen cooling. Experimental temperature curves are depicted in Figure 1(b). 2 to 3 steel samples were collected with each cooling method for microscopic investigation. The central and side parts of the steel ingots from the alumina crucible after furnace cooling, air cooling, and water cooling processes were machined into metallographic samples (15 mm × 15 mm × 15 mm) for microscopic investigation. A quartz tube was also used to collect the samples of liquid steel (Φ5 mm × 100 mm) which were then immediately quenched in water and liquid nitrogen, respectively. Cooling types, sampling methods and cutting positions of the experimental steel samples are summarized in Table II.

### B. Specimen Analysis

Inductively coupled plasma optical emission spectrometry (ICP-OES) was used to quantitatively measure the chemical compositions of the non-quenched and tempered steel samples. A cross section of each steel sample was ground with SiC abrasive paper and then polished with diamond suspension. Characteristics of MnS inclusions in the steel samples, including chemical compositions, morphologies, average diameters, size distributions and number densities, were measured by scanning electron microscopy and energy dispersive spectrometry (SEM–EDS) with an Aspek Explorer

**Table I. Chemical Composition of the Non-quenched and Tempered Steel**

Element	Mn	Si	S	P	Al	Cr	V	C	N	T.O
Content (mass pct)	1.34	0.39	0.045	0.015	0.011	0.14	0.08	0.45	0.013	0.0015

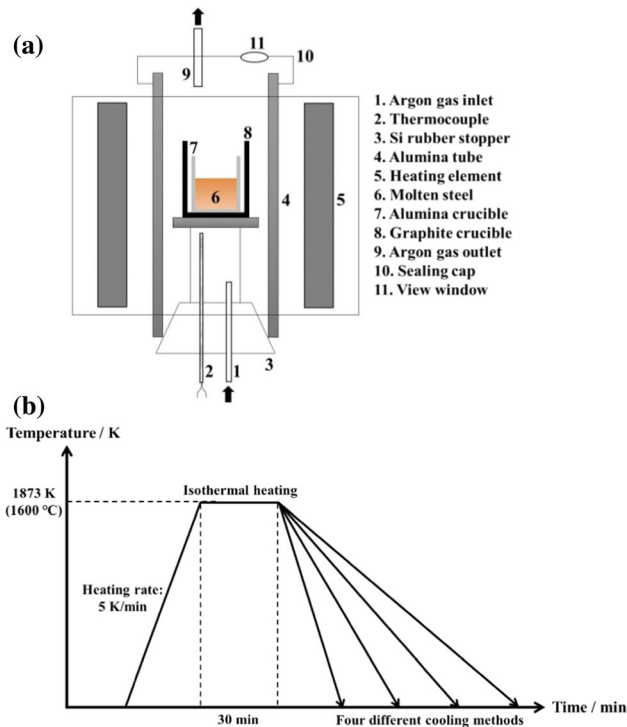


Fig. 1—Schematic diagram of (a) experimental apparatus and (b) experimental temperature curves.

**Table II. Cooling Types, Sampling Methods and Cutting Positions of the Experimental Steel Samples**

Steel Sample No.	Cooling Type	Sampling Method and Cutting Position
S1	furnace cooling	crucible, centric position
S2	furnace cooling	crucible, edge position
S3	air cooling	crucible, centric position
S4	air cooling	crucible, edge position
S5	water cooling	crucible, centric position
S6	water cooling	crucible, edge position
S7	water cooling	quartz tube
S8	liquid nitrogen cooling	quartz tube

instrument. (accelerating voltage: 10 kV,<sup>[18]</sup> spot size: 40 pct, brightness: 5 to 7 pct, contrast: 100 pct). At least 16 mm<sup>2</sup> of analysis area for each sample was performed to acquire sufficient data. Experimental steel samples with different cooling approaches were etched with hydrochloric acid aqueous solution and also observed under the scanning electron microscopy. The metallographic morphologies of those steel samples were analyzed and the average secondary dendrite arm spacing (SDAS) of each steel sample was measured.

### III. RESULTS

Figure 2 shows the morphologies of typical MnS inclusions in different steel samples after solidification experiments with various cooling methods. As presented in Figure 2, in all cases, MnS inclusions generally precipitated

as standalone particles with different average sizes. From steel samples S1 to S7, the average diameter and number density of MnS inclusions represented a decreasing and an increasing trend, respectively, as shown in Figure 3. The average diameter decreased from 9.35 to 1.83 μm and the number density increased from 81 to 587 mm<sup>-2</sup>. Nevertheless, although the steel sample S8 used the same sampling method (quartz tube) as the steel sample S7, instead of water, liquid nitrogen as the coolant resulted in a lower number density and a similar average size of MnS inclusions in the steel which were 454 mm<sup>-2</sup> and 1.94 μm, respectively. In addition, by comparison of different steel samples with the same cooling method, the results showed that the effect sequence of the sampling method on contributing to the fineness and dispersion of MnS inclusions was as follows: sampling by quartz tube > sampling at the edge part of the steel ingot > sampling at the central part of the steel ingot.

Figure 4 shows the size distributions of MnS inclusions in different steel samples after solidification experiments with various cooling methods. As presented in Figure 4, in the steel samples S1 and S2 after furnace cooling, the diameters of MnS inclusions smaller than 10 μm are evenly distributed in the range of 0 to 10 μm with the interval of 1.0 μm which have average number densities of about 7.2 and 5.1 mm<sup>-2</sup>, respectively, while those larger than 10 μm account for approximate 30 pct of the total inclusions in both cases where their average number densities reach 26.9 and 30.2 mm<sup>-2</sup>, respectively. The sizes of MnS inclusions in the steel samples S3 and S4 after air cooling are mainly distributed in the range of 0 to 5 μm, and the number densities of large-sized MnS inclusions (> 10 μm) decrease obviously by comparison with those in the steel samples S1 and S2. In the steel samples S5 to S8 after quenching in water and liquid nitrogen, most of MnS inclusions become much smaller and are mainly distributed in the range of 0 to 3 μm, and no MnS inclusions larger than 10 μm were found, although their number densities increased significantly, especially for the smaller ones (0 to 3 μm).

Experimental steel samples S1 to S8 then went through hot etching tests with 20 pct hydrochloric acid aqueous solution for 5 to 10 minutes. The metallographic morphologies of those steel samples were analyzed and the average SDAS of each steel sample was measured. Quantitative relationships between the cooling rate and secondary dendrite arm spacing were employed,<sup>[19]</sup> as shown in Eqs. [1] and [2].

$$\lambda_1 = (169.1 - 720.9[C]) \cdot R_c^{-0.4935}, 0 < [C] \leq 0.15 \text{ pct} \quad [1]$$

$$\lambda_2 = 143.9R_c^{-0.316} \cdot [C]^{(0.5501-1.996[C])}, [C] > 0.15 \text{ pct}, \quad [2]$$

where λ is the secondary dendrite arm spacing, μm; R<sub>c</sub> is the cooling rate, K/s; [C] is the carbon concentration in the steel, mass pct. By taking S4 steel sample as an example, the morphologies of the primary and secondary dendrites, and the measurement method of the secondary dendrite arm spacing is shown in Figure 5. Average SDAS measurement results and corresponding cooling rates for steel samples S1 to S8 are

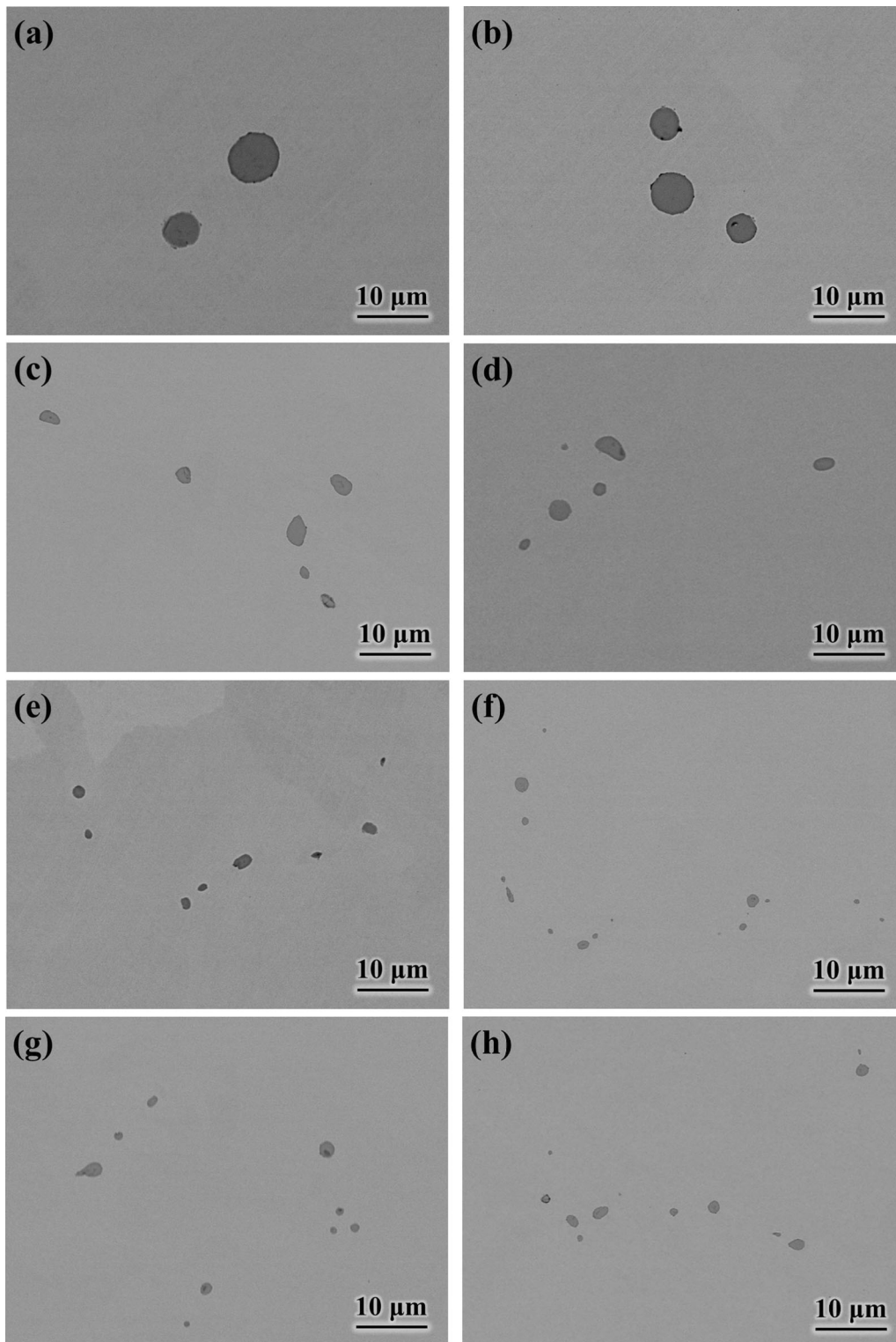


Fig. 2—Morphologies of typical MnS inclusions in different steel samples: (a) S1; (b) S2; (c) S3; (d) S4; (e) S5; (f) S6; (g) S7; (h) S8.

summarized in Table III. Experimental and calculated results reported a decreasing trend in the SDAS from the steel sample S1 (174.8  $\mu\text{m}$ ) to S8 (44.3  $\mu\text{m}$ ) and the corresponding cooling rate increased from 1.26 to 56.01  $\text{K s}^{-1}$ .

Figure 6 depicts the relationship between the cooling rate of molten steel and average inclusion diameter based on experimental and calculated results. A non-linear fitting curve was acquired, and the coefficient of

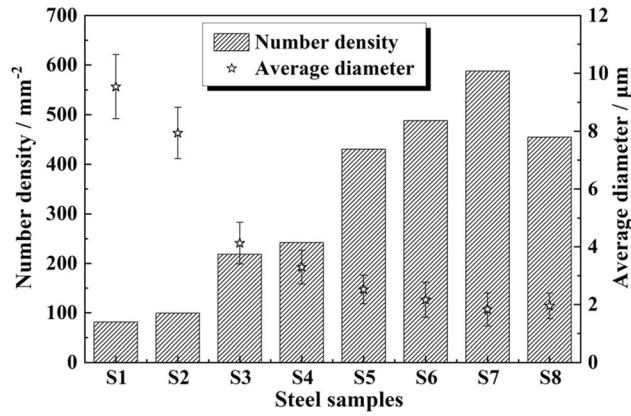


Fig. 3—Number densities and average diameters of MnS inclusions in different steel samples.

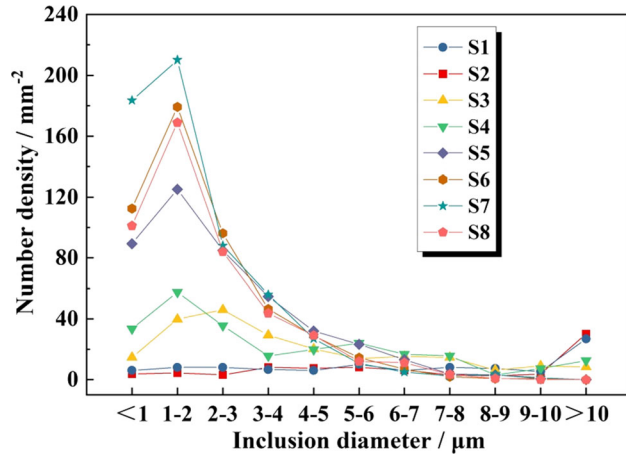


Fig. 4—Size distributions of MnS inclusions in different steel samples.

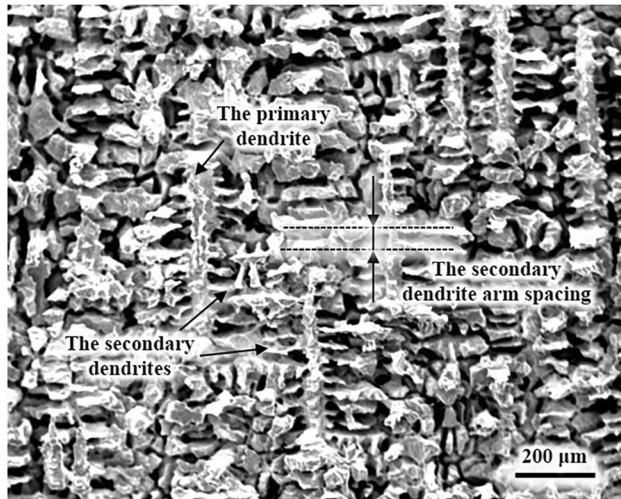


Fig. 5—Morphologies of the primary and secondary dendrites, and the measurement method of the secondary dendrite arm spacing (taking S4 steel sample as an example).

determination ( $R^2$ ) of the fitting curve equation, as shown in Eq. [3], reached 0.9914, which demonstrated its high precision.

Table III. Measured Secondary Dendrite Spacings and Calculated Cooling Rates of the Steel Samples

Steel Sample No.	Average Secondary Dendrite Spacing ( $\mu\text{m}$ )	Cooling Rate ( $\text{K s}^{-1}$ )
S1	174.8	1.26
S2	145.3	2.10
S3	83.9	9.58
S4	70.2	15.68
S5	60.2	23.94
S6	51.9	36.11
S7	49.0	42.35
S8	44.3	56.01

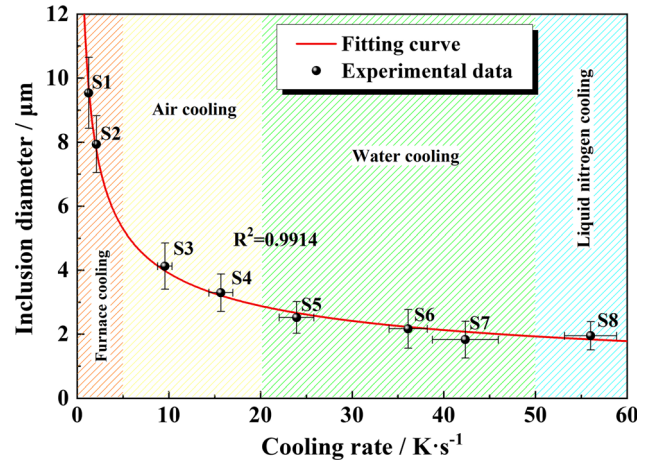


Fig. 6—Relationship between the cooling rate of molten steel and average inclusion diameter based on experimental and calculated results.

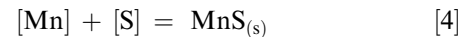
$$d = 10.726v^{-0.438}, \quad [3]$$

where  $d$  is the average diameter of MnS inclusions,  $\mu\text{m}$ ;  $v$  represents the cooling rate of molten steel,  $\text{K s}^{-1}$ .

## IV. DISCUSSION

### A. Establishment of the Solute Element Segregation Models

The chemical reaction of MnS inclusion precipitation in the non-quenched and tempered steel is shown in Eq. [4], and the related temperature dependence of standard Gibbs free energy change is given in Eq. [5], respectively.



$$\begin{aligned} \Delta G^\circ &= -RT \cdot \ln K_{\text{MnS}} \\ &= -158365 + 93.996T \quad (\text{J mol}^{-1}), \end{aligned} \quad [5]$$

where  $K_{\text{MnS}}$  represents the equilibrium constant, and  $T$  represents the temperature of molten steel, K;  $R$  represents the ideal gas constant of  $8.314 \text{ J mol}^{-1} \text{ K}^{-1}$ .

The actual change of Gibbs free energy can be calculated by Eq. [6] regarding to the precipitation of MnS inclusions.

$$\begin{aligned}\Delta G &= \Delta G^\circ + RT \ln \frac{a_{\text{MnS}}}{a_{[\text{Mn}]} \cdot a_{[\text{S}]}} \\ &= \Delta G^\circ + RT \ln \frac{1}{f_{\text{Mn}} \cdot \omega_{[\text{Mn}]} \cdot f_{\text{S}} \cdot \omega_{[\text{S}]}}\end{aligned}\quad [6]$$

where  $a_{\text{MnS}}$ ,  $a_{[\text{S}]}$  and  $a_{[\text{Mn}]}$  represent the activities of MnS, S and Mn in liquid steel, respectively. For pure MnS,  $a_{\text{MnS}} = 1$ .  $\omega_{[\text{Mn}]}$  and  $\omega_{[\text{S}]}$  represent the mass fraction of Mn and S in liquid steel, respectively;  $f_{\text{Mn}}$  and  $f_{\text{S}}$  represent the activity coefficients of Mn and S, respectively which can be calculated by Eqs. [7] and [8].<sup>[20]</sup>

$$\log f_i^T = \left( \frac{2538}{T} - 0.355 \right) \cdot \log f_i^{1873\text{K}} \quad [7]$$

$$\log f_i^{1873\text{K}} = e_i^j[\text{pct } i] + \sum e_i^j[\text{pct } j], \quad [8]$$

where  $f_i^{1873\text{K}}$  is the activity coefficient of solute element  $i$  at 1873 K (1600 °C), [pct  $i$ ] and [pct  $j$ ] are the concentrations of solute elements  $i$  and  $j$ , pct. For the studied non-quenched and tempered steel, the first-order interaction coefficients of main solute elements with Mn and S elements in the molten steel at 1873 K (1600 °C) are listed in Table IV.<sup>[21,22]</sup> The influence of the second-order interaction coefficients can be neglected since the mass fraction of Fe in the molten steel is greater than 90 pct.

By combining Eqs. [4] through [8], as the solidification proceeds, the temperature of molten steel decreases which leads to the variation of actual Gibbs free energy change  $\Delta G$ . If  $\Delta G$  is equal or lesser than 0, MnS precipitation becomes feasible thermodynamically. According to the Eqs. [4] through [6], the thermodynamic conditions of MnS precipitation are described in Eq. [9].

$$K_{\text{MnS}}^* \leq Q_{\text{MnS}} = f_{\text{Mn}} \cdot \omega_{[\text{Mn}]} \cdot f_{\text{S}} \cdot \omega_{[\text{S}]}, \quad [9]$$

where  $K_{\text{MnS}}^*$  is the activity product of Mn and S elements at chemical equilibrium, which can be calculated by  $K_{\text{MnS}}$ , and  $Q_{\text{MnS}}$  is the activity product of Mn and S elements in molten steel at a certain time during solidification. Owing to the micro-segregations of solute elements in different degrees during the solidification process of molten steel, some parameters in the above equations will vary as the solidification proceeds. Thus, the precise determination of the concentration variations of solute elements during solidification is a key point.

In this study, two models, Clyne–Kurz model and Ohnaka model,<sup>[16,17]</sup> were introduced to evaluate the micro-segregations of solute C, N, O, Si, Mn, P, Ti and S elements, respectively. The calculation results are also compared and analyzed. Figure 7 shows the schematic diagram of microscopic solidification process of steel and calculation unit introduced in the finite volume method for micro-segregations of solute elements. The calculation unit began from the central axis of one secondary dendrite arm and ended up with the symmetric line of one secondary dendrite arm space. Thus, one calculation unit consisted of three parts, solid phase region, liquid phase region, and solidification front. The calculation using finite volume method was conducted by every solidification fraction of 0.001 on the assumption that the solidification process and temperature of molten steel were in quasi-steady states. During solidification, the solid–liquid interface gradually shifted towards the interdendritic molten steel pool.

The real-time concentrations of different solute elements at the solidification front can be calculated by Eq. [10] as the solidification proceeds:

$$\omega_{[i]} = [1 - (1 - \theta k_i)g]^{(k_i-1)/(1-\theta k_i)} \cdot \omega_{[i]}^0, \quad [10]$$

where  $\omega_{[i]}$  is the real-time concentration of solute element  $i$  at the solidification front, mass pct;  $\omega_{[i]}^0$  is the concentration of solute element  $i$  in molten steel before solidification, mass pct;  $g$  is the solidification fraction;  $k_i$  is the partition coefficient of solute element  $i$  in steel, which can be obtained from Table V.<sup>[23–26]</sup>  $\theta$  is a modified diffusion parameter to conform to related boundary conditions for predicting the solidification behavior of molten steel which can be calculated by Eqs. [11] and [12] in the Clyne–Kurz and Ohnaka models, respectively.<sup>[16,17]</sup>

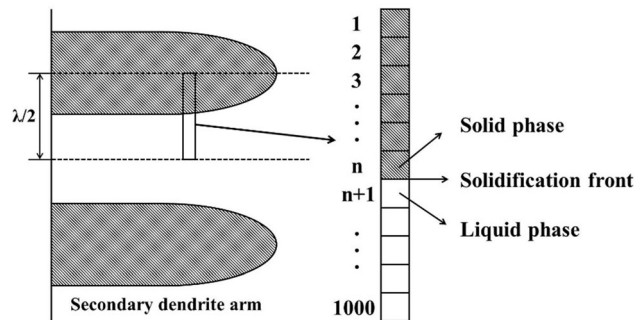


Fig. 7—Schematic diagram of microscopic solidification process of steel and calculation unit introduced in the finite volume method for micro-segregations of solute elements.

Table IV. Interaction Coefficients of Main Elements with Mn and S Elements in Steel at 1873 K (1600 °C)

$e_i^j$	C	Si	Mn	P	S	N	Cr	Al	V	O
Mn	− 0.0538	− 0.0327	0	− 0.06	− 0.048	− 0.091	0.0039	0.027	—	− 0.087
S	0.112	0.063	− 0.026	0.29	− 0.028	0.01	− 0.011	0.035	− 0.016	− 0.27

**Table V. Partition Coefficients of Solute Elements Between Solid and Liquid Steels and Their Diffusion Coefficients in Solid Steel**

Element	$k_i$	$D_i^s$ (cm <sup>2</sup> s <sup>-1</sup> )
C	0.34	0.15Exp (- 143,511/RT <sub>l-s</sub> )
Si	0.52	0.3Exp (- 251,458/RT <sub>l-s</sub> )
Mn	0.78	0.055Exp (- 249,366/RT <sub>l-s</sub> )
P	0.13	0.01Exp (- 182,841/RT <sub>l-s</sub> )
S	0.035	2.4Exp (- 223,426/RT <sub>l-s</sub> )
N	0.48	0.91Exp (- 168,490/RT <sub>l-s</sub> )
Cr	0.86	0.0012Exp (- 218,991/RT <sub>l-s</sub> )
Al	0.6	5.9 Exp (- 241,417/RT <sub>l-s</sub> )
V	0.63	0.284Exp (- 258,990/RT <sub>l-s</sub> )
O	0.025	5.75Exp (- 168,615/RT <sub>l-s</sub> )

$$\text{Clyne - Kurz model : } \emptyset = 2\alpha \left(1 - e^{-1/\alpha}\right) - e^{-1/2\alpha} \quad [11]$$

$$\text{Ohnaka Model : } \emptyset = \frac{4\alpha}{1 + 4\alpha}, \quad [12]$$

where  $\alpha$  is an inverse diffusion coefficient and can be obtained by Eq. [13]:

$$\alpha = 4D_i^s\tau/\lambda^2, \quad [13]$$

where  $D_i^s$  is the diffusion coefficient of solute element  $i$  in solid steel, cm<sup>2</sup> s<sup>-1</sup>, which are listed in Table V.  $\tau$  is the local solidification time of molten steel,  $s$ , which can be calculated by Eqs. [14] through [16].

$$\tau = \frac{T_l - T_s}{R_c} \quad [14]$$

$$T_l = T_{Fe} - \sum \Delta\Gamma_l \cdot \omega_{[i]} \quad [15]$$

$$T_s = T_{Fe} - \sum \Delta\Gamma_s \cdot \omega_{[i]}, \quad [16]$$

where  $R_c$  denotes the cooling rate of molten steel, K s<sup>-1</sup>;  $T_s$  denotes the solidus temperature, K;  $T_l$  denotes the liquidus temperature, K;  $\Delta\Gamma_l$  and  $\Delta\Gamma_s$  denote the reduced liquidus and solidus temperature values for 1.0 mass pct solute element  $i$  in molten steel, respectively, which can be found in Table VI.<sup>[27,28]</sup>  $T_{Fe}$  is the melting point of molten iron, which was taken as 1811 K (1538 °C) in this study.

The solidification front temperature  $T_{l-s}$  is a function of solidus temperature, liquidus temperature and solidification fraction, which can be calculated by Eq. [17]:

$$T_{l-s} = T_{Fe} - \frac{T_{Fe} - T_l}{1 - \frac{T_l - T_s}{T_{Fe} - T_s} \cdot g} \quad [17]$$

To estimate the MnS inclusion size after complete solidification of molten steel, the main limitation factors for controlling MnS precipitation and growth should be clear. It was assumed that the MnS growth was generally controlled by Mn and S diffusion from the molten steel to the solidification front, since the chemical reaction rate at the MnS-steel interface is high enough at the temperature of molten steel. The diffusion coefficients of Mn and S,  $D_{Mn}^l$  and  $D_S^l$ , in the molten steel can be computed in Eqs. [18] and [19], respectively:<sup>[12,25,29,30]</sup>

$$D_{Mn}^l (\mu\text{m}^2/\text{s}) = 1.8 \times 10^5 \text{Exp}(-13,000/RT) \quad [18]$$

$$D_S^l (\mu\text{m}^2/\text{s}) = 4.33 \text{Exp}(-35,600/RT) \quad [19]$$

Equations [18] and [19] demonstrate that the diffusion coefficient of sulfur element is much smaller than that of manganese element within the temperature range of molten steel. Beside, in the molten steel, the original sulfur content is about two orders of magnitude lower than that of Mn element, as exhibited in Table I. Thus, the growth of MnS inclusion was deemed to be controlled by the S diffusion in steel. For a certain MnS particle with the radius of  $r$ , the diffusion flux of S element can be obtained by Eq. [20].

$$J_S = \frac{D_S^l \cdot \rho_{Fe}}{100M_S \cdot r} \cdot \left(\omega'_{[S]} - \omega^*_{[S]}\right), \quad [20]$$

where  $J_S$  is the diffusion flux of S element, mol m<sup>-2</sup> s<sup>-1</sup>;  $\rho_{Fe}$  is the density of iron which was assumed to be  $7.87 \times 10^3$  kg m<sup>-3</sup>;  $M_S$  is the molar mass of S element, kg mol<sup>-1</sup>;  $\omega'_{[S]}$  is the calculated concentration of S element by coupling S micro-segregation and MnS precipitation during solidification, mass pct;  $\omega^*_{[S]}$  is the concentration of S element at the chemical reaction equilibrium with MnS inclusion, mass pct;  $r$  is the radius of MnS inclusion,  $\mu\text{m}$ .

In the process of modeling, MnS inclusions are assumed to be spherical and grow independently without interaction with others. Then the relationship between the diffusion flux of S and the radius of MnS inclusion can be expressed by Eq. [21]:

$$4\pi r^2 \cdot M_{MnS} \cdot J_S \cdot \Delta t = \frac{4}{3}\pi \cdot \rho_{MnS} \cdot \left[(r + \Delta r)^3 - r^3\right], \quad [21]$$

where  $M_{MnS}$  is the molar mass of MnS, kg mol<sup>-1</sup>;  $\rho_{MnS}$  is the density of MnS phase ( $4.04 \times 10^3$  kg m<sup>-3</sup>);  $\Delta t$  is the unit growth time, s, and  $\Delta r$  is the increase in MnS inclusion radius per unit growth time,  $\mu\text{m}$ . Thus, by combining Eqs. [20] and [21], the change in MnS inclusion size during solidification can be obtained by Eq. [22].

$$\int_0^{r_i} r dr = \int_0^t \frac{M_{MnS} \cdot \rho_{Fe}}{100M_S \cdot \rho_{MnS}} \cdot D_S^l \cdot \left(\omega'_{[S]} - \omega^*_{[S]}\right) dt \quad [22]$$

Table VI.  $\Delta\Gamma_l$  and  $\Delta\Gamma_s$  Values of Solute Elements in Molten Steel

Element	S	N	Mn	P	C	Si	Cr	Al	V	O
$\Delta\Gamma_l$ (K)	25	90	5	30	65	7.8	1.5	2.7	2	80
$\Delta\Gamma_s$ (K)	575	—	6.8	280	175	12.3	1.4	7.5	—	160

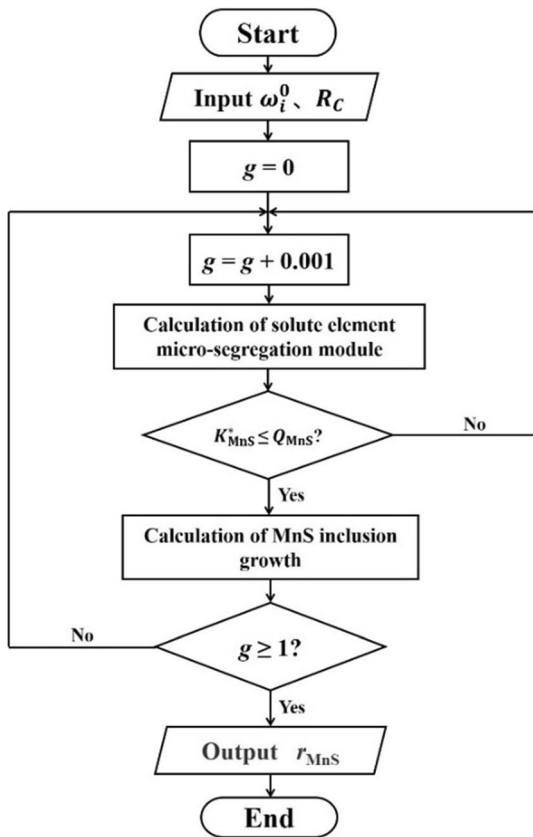


Fig. 8—The whole flow chart of the model calculations on precipitation and growth of MnS inclusion during solidification.

Figure 8 displays the whole flow chart of the model calculations on precipitation and growth of MnS inclusion during solidification. It should be noted that in this model calculation, the generation and precipitation of other types of inclusions such as oxides, nitrides, and carbides were not taken into consideration, since in this non-quenched and tempered steel, MnS inclusion (including oxysulfide inclusions) accounts for over 98 pct in the total inclusions. The consumptions of those solute elements due to the precipitation of other types of inclusions would have little influence on the calculation results in the solute micro-segregation models.

### B. Calculation Results of Solute Elements Micro-segregations

Calculations on the micro-segregation ratios and concentrations of solute elements during solidification ( $R_c = 1.26 \text{ K s}^{-1}$ , steel sample S1) were performed in the improved Clyne–Kurz and Ohnaka models, as

shown in Figure 9. Since the micro-segregations of Mn and S probably would be influenced by the precipitation and growth of MnS inclusions, their results were temporarily not discussed here. Calculation results in Figures 9(a) and (c) demonstrated that variations of solute segregation ratios with solidification fraction predicted by Clyne–Kurz and Ohnaka models were highly similar. As the solidification proceeds, the micro-segregation ratios of O and P increased obviously, especially in the late stage, while those of Si, C, V, N, Cr, and Al varied gently and were also very close to each other in both Clyne–Kurz and Ohnaka models. Generally, the sequence of the micro-segregation ratios of these solute elements is  $O > P > Si > C > V > N > Cr > Al$ , although at the end of solidification, the micro-segregation ratio of C is slightly higher than that of Si in the Ohnaka model. Figures 9(b) and (c) display the variations of solute element concentrations with solidification fraction calculated by Clyne–Kurz and Ohnaka models. Although the segregation ratios of C and Si after solidification were relatively low (around 3.0) among the solute elements, the C and Si concentrations increased obviously since the initial C and Si concentrations in the liquid steel were relatively high (0.45 and 0.39 mass pct, respectively), while the concentrations of other solute elements increased slightly due to their low initial concentrations ( $< 0.14$  mass pct). Thus, effects of the micro-segregations of C and Si during solidification on the thermodynamic parameters including  $T_l$ ,  $T_s$ ,  $T_{l-s}$ , and  $\lambda$  should be taken into consideration seriously.

### C. Thermodynamic Calculation of MnS Precipitation and Growth

The micro-segregation ratios and concentrations of solute Mn and S elements during solidification ( $R_c = 1.26 \text{ K s}^{-1}$ , steel sample S1) calculated by the improved Clyne–Kurz and Ohnaka models are shown in Figure 10. In the thermodynamic calculation results, the solid lines represented the micro-segregation ratios and concentrations of solute Mn and S elements by taking MnS precipitation into account, while the dash lines represented those of Mn and S elements without considering MnS precipitation during solidification. Those inflection points denoted the solidification fractions where the precipitation of MnS inclusion started. The variation trends of the calculated results by Clyne–Kurz and Ohnaka models were still quite similar, although there was only a little difference in their absolute values. Taking the data by Clyne–Kurz model calculation as an example, as shown in Figures 10(a) and (b), without considering MnS precipitation, the



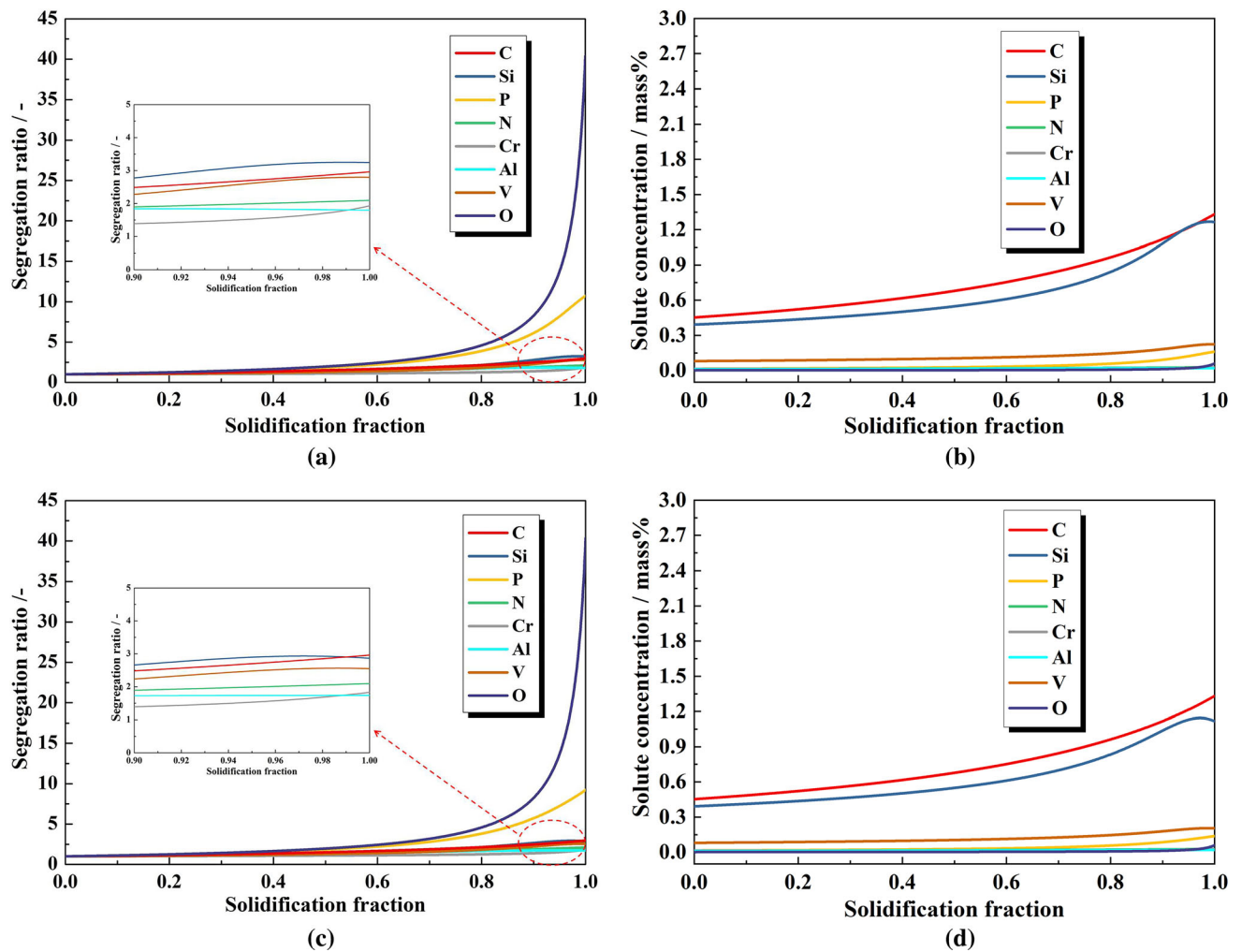


Fig. 9—Variations in (a) segregation ratios and (b) concentrations of solute elements with solidification fraction calculated by Clyne–Kurz model; and variations in (c) segregation ratios and (d) concentrations of solute elements calculated by Ohnaka model.

micro-segregation ratios of Mn and S would increase to 2.19 and 29.9, and their concentrations would reach 2.93 and 1.35 mass pct as the solidification proceeded, respectively. However, when the micro-segregation model was coupled with the MnS precipitation module, the micro-segregations of Mn and S elements were alleviated and the calculated results would be quite different. The micro-segregation ratios of Mn and S elements increased to 1.78 and 9.94 first, and then decreased to 0.82 and 6.13, respectively, and their concentrations increased to 2.39 and 0.45 mass pct first, and then decreased to 1.09 and 0.28 mass pct, respectively.

Figure 11 shows the changes of liquidus, solidus and solidification front temperatures with solidification fraction calculated by the improved Clyne–Kurz and Ohnaka models. Results show that with the increase of solidification fraction, the liquidus and solidus temperatures decreased due to the micro-segregations of solute elements, as shown in Figures 11(a) and (c). Compared with that of the liquidus temperature, the

decreasing rate of the solidus temperature was much larger, especially at the end of the solidification. Thus, the temperature range for the mushy region of liquid steel was enlarged which resulted in the decline of the solidification front temperature to approximate 1653 K (1380 °C), as shown in Figures 11(b) and (d).

Figure 12 shows the variations of theoretical equilibrium activity product  $K_{\text{MnS}}^*$  and actual activity product  $Q_{\text{MnS}}$  with solidification fraction calculated by the improved Clyne–Kurz model and Ohnaka model. As the solidification proceeds, the theoretical equilibrium activity product  $K_{\text{MnS}}^*$  as a function of the solidification front temperature  $T_{l-s}$  gradually decreased, while the actual activity product  $Q_{\text{MnS}}$  gradually increased. The solidification fraction points for MnS precipitation where the  $Q_{\text{MnS}}$  became larger than the  $K_{\text{MnS}}^*$  in the Clyne–Kurz and Ohnaka models were 0.929 and 0.931, respectively. After MnS precipitation, the actual activity product  $Q_{\text{MnS}}$  descended and kept closely with the theoretical equilibrium activity product  $K_{\text{MnS}}^*$ .

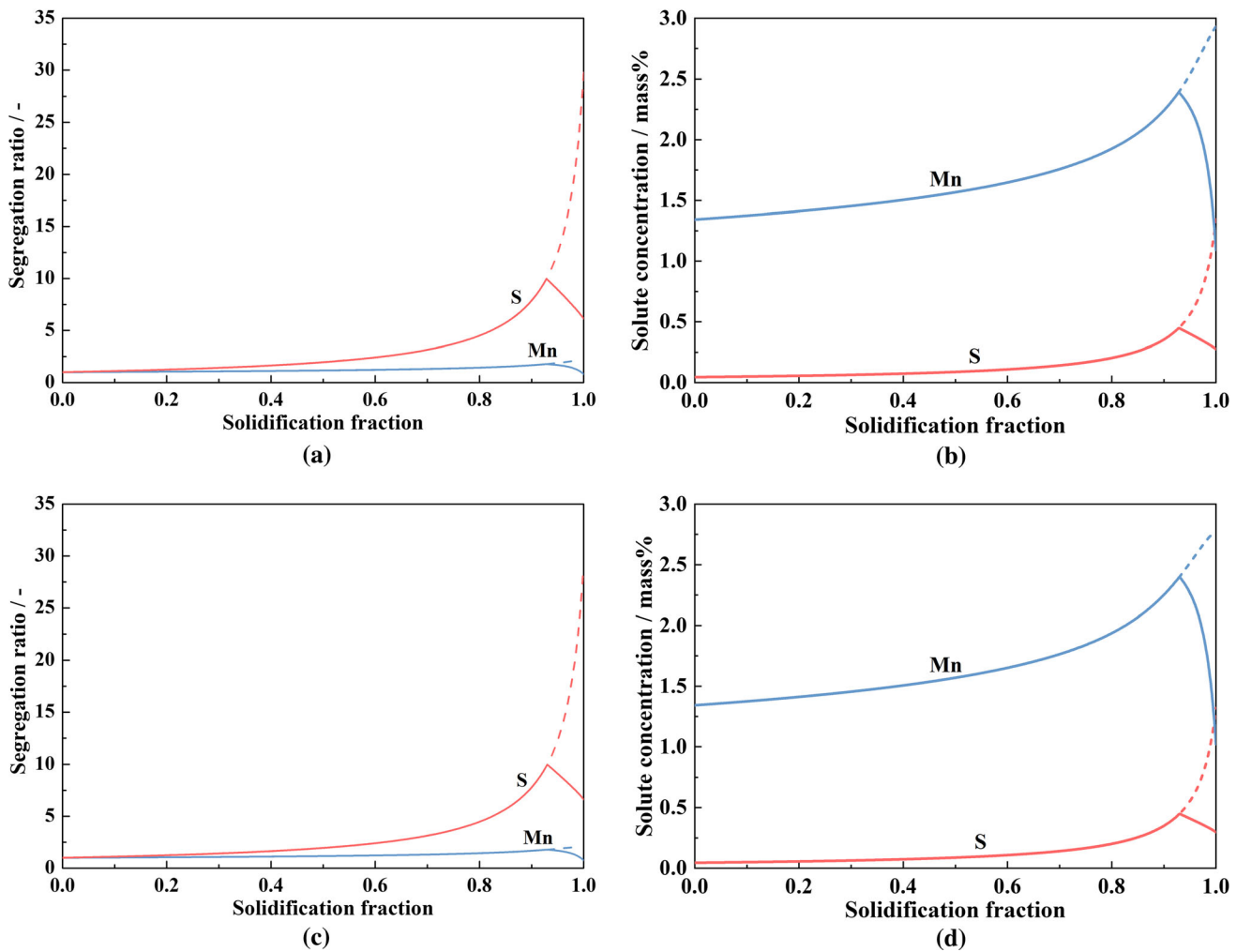


Fig. 10—Variations in (a) segregation ratios and (b) concentrations of Mn and S elements with solidification fraction calculated by Clyne–Kurz model; and variations in (c) segregation ratios and (d) concentrations of Mn and S elements calculated by Ohnaka model.

Figure 13 shows the relationships among inclusion diameter, cooling rate and solidification time by comparison of experimental results and model calculations with and without the effects of micro-segregation of other solute elements including silicon, phosphorus, oxygen, nitrogen and so on. Calculated sizes of the MnS particles after steel solidification upon the cooling rate in the improved Clyne–Kurz and Ohnaka models are quite similar and consistent with the experimental data, while as the effects of micro-segregation of other solute elements are not taken into consideration, the diameters of MnS inclusions in the two models are overestimated and deviate from the experimental results, as shown in Figure 13(a). At the early state of the solidification, when the actual activity product  $Q_{\text{MnS}}$  was lower than the theoretical equilibrium activity product  $K_{\text{MnS}}^*$ , no MnS inclusion precipitated within a period of time for each case. As the solidification proceeded, when  $K_{\text{MnS}}^* \leq Q_{\text{MnS}}$ , MnS particles started to precipitate. The growth of MnS inclusions during solidification was estimated by model calculations with the effects of micro-segregation of other solute elements, and the

calculation results by the improved Clyne–Kurz and Ohnaka models were in reasonable agreement with the experimental data, as shown in Figure 13(b).

Those findings in the experiments and model calculations have fully revealed the quantitative relationships among the cooling method, cooling rate, and MnS inclusion size. In the industrial continuous casting production, the processing parameters including spray water rate and pulling rate can be accordingly optimized to precisely control the size distribution of MnS inclusions in the cross section of the slab and suppress the mechanical anisotropy of steel caused by the elongated MnS inclusions after hot rolling.

## V. CONCLUSIONS

- (1) Depending on different cooling and sampling methods, the number density and average size of MnS inclusions in this non-quenched and tempered steel obviously have a positive and a negative cor-

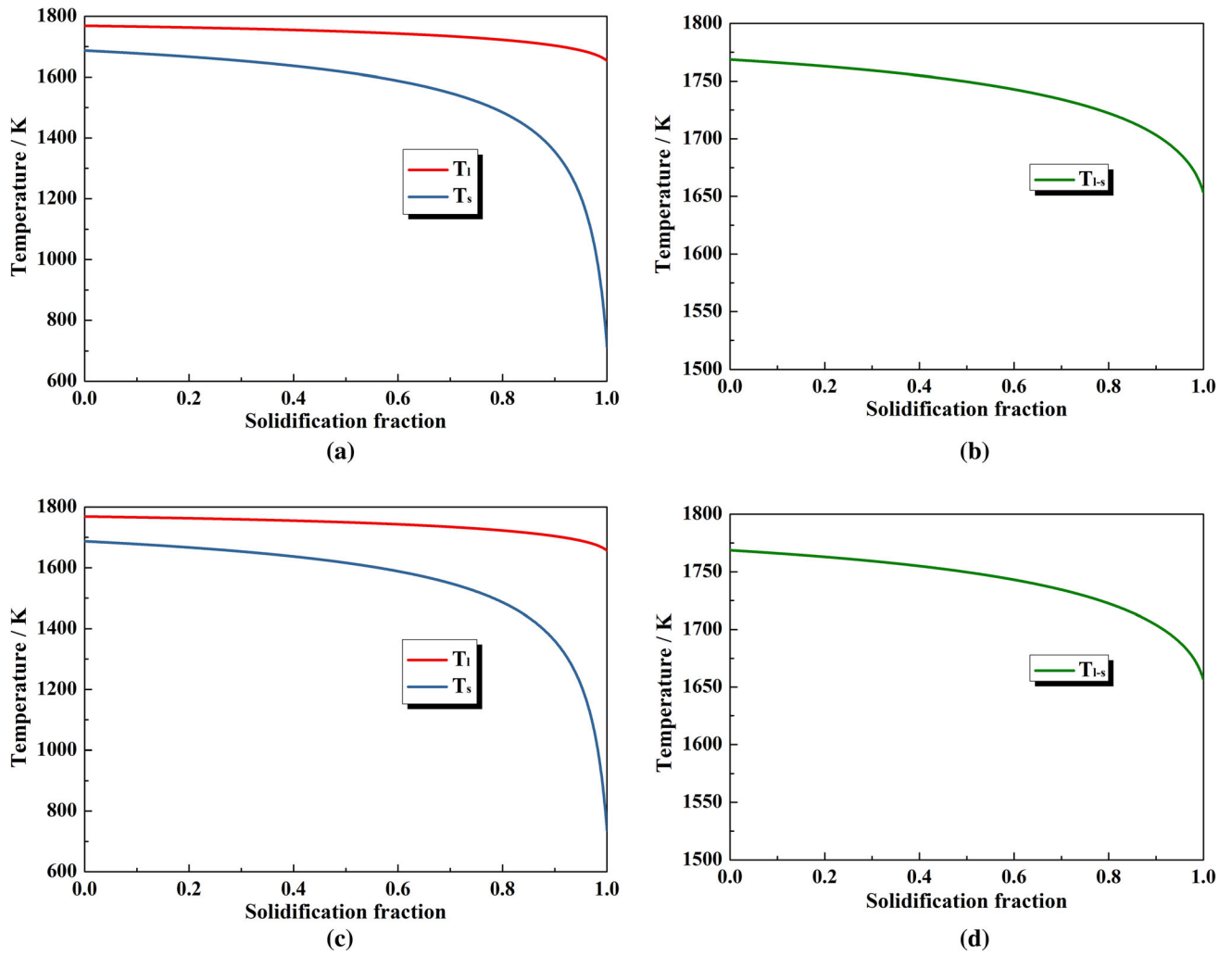


Fig. 11—Changes of (a) liquidus temperature, solidus temperature and (b) solidification front temperature with solidification fraction obtained by Clyne–Kurz model, and changes of (c) liquidus temperature, solidus temperature and (d) solidification front temperature with solidification fraction obtained by Ohnaka model.

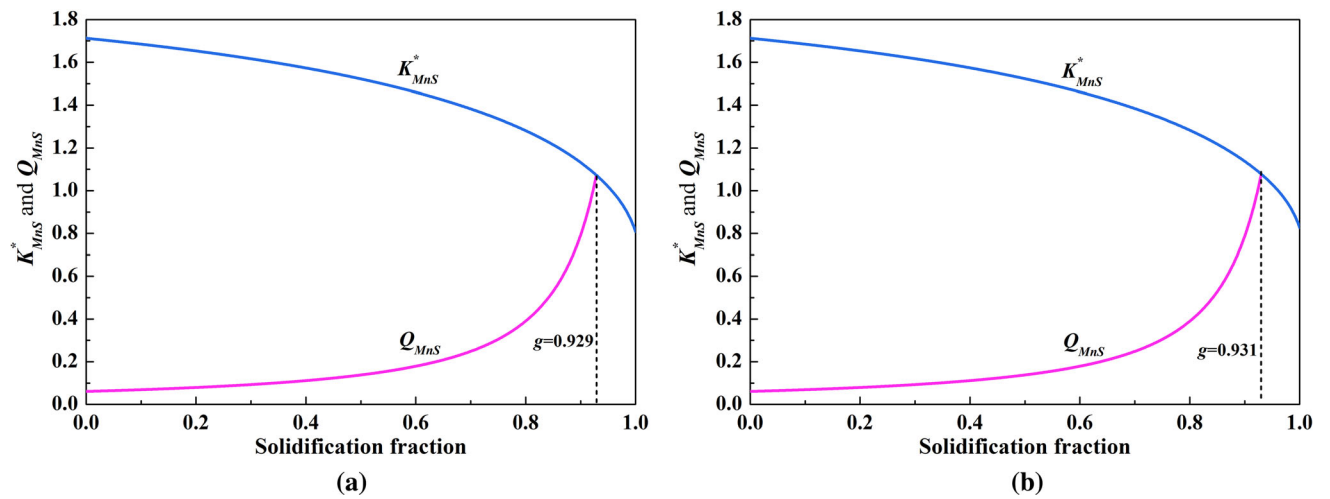


Fig. 12—Variations of actual concentration product and theoretical concentration product with solidification fraction calculated by (a) Clyne–Kurz model and (b) Ohnaka model.

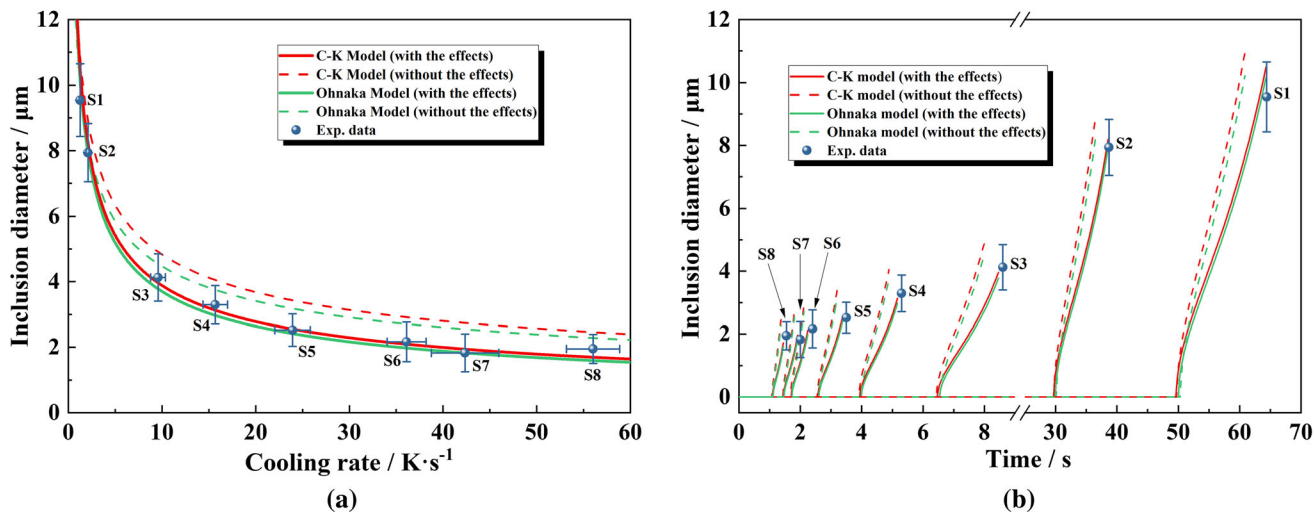


Fig. 13—Comparison of model calculations and experimental results of inclusion size variation with different cooling rates: (a) relationship between cooling rate and inclusion diameter; (b) relationship between solidification time and inclusion diameter.

relation with the cooling rate, respectively. A non-linear fitting curve equation to describe the relationship between cooling rate of molten steel  $v$  and average inclusion diameter  $d$  was acquired by solidification experiments:  $d = 10.726v^{-0.438}$ .

- (2) Thermodynamic calculation results by the improved Clyne–Kurz and Ohnaka models on MnS precipitation and growth behaviors including micro-segregation ratios and concentrations of solute elements, liquidus, solidus and solidification front temperatures, etc., were quite similar. At the cooling rate of  $R_c = 1.26 \text{ K s}^{-1}$ , the solidification fraction values for MnS precipitation in the two models were 0.929 and 0.931, respectively.
- (3) Precipitation and growth behaviors of MnS inclusions during solidification were well predicted by the improved Clyne–Kurz and Ohnaka solute element micro-segregation models on the basis of experimental and calculated results. Both the two models were validated and could be judged as equivalent in this work.

### ACKNOWLEDGMENTS

The current study was supported by the National Natural Science Foundation of China (Grant no. 52074198).

### CONFLICT OF INTEREST

On behalf of all authors, the corresponding author states that there is no conflict of interest.

### REFERENCES

1. B. Jiang, W. Fang, R.M. Chen, D.Y. Guo, Y.J. Huang, C.L. Zhang, and Y.Z. Liu: *Mat. Sci. Eng. A*, 2019, vol. 748, pp. 180–88.

2. Y. Yang, C.B. Lai, F.M. Wang, Z.B. Yang, and B. Song: *Int. J. Min. Met. Mater.*, 2007, vol. 14, pp. 501–06.
3. K. Wang, T. Yu, Y. Song, H.X. Li, M.D. Liu, R. Luo, J.Y. Zhang, F.S. Fang, and X.D. Lin: *Metall. Mater. Trans. B*, 2019, vol. 50B, pp. 1213–24.
4. T.F. Majka, D.K. Matlock, and G. Krauss: *Metall. Mater. Trans. A*, 2002, vol. 33A, pp. 1627–37.
5. J. Torkkeli, T. Saukkonen, and H. Hanninen: *Corros. Sci.*, 2015, vol. 96, pp. 14–22.
6. P.A. Thornton: *J. Mater. Sci.*, 1971, vol. 6, pp. 347–56.
7. J.C. Yan, T. Li, Z.Q. Shang, and H. Guo: *Mater. Charact.*, 2019, p. 109944.
8. K. Oikawa, K. Ishida, and T. Nishizawa: *ISIJ Int.*, 1997, vol. 37, pp. 332–38.
9. H. Takada, I. Bessho, and T. Ito: *Tetsu to Hagane*, 1978, vol. 62, pp. 1319–28.
10. M.L. Li, F.M. Wang, C.R. Li, Z.B. Yang, Q.Y. Meng, and S.F. Tao: *Int. J. Miner. Metall.*, 2015, vol. 22, pp. 589–97.
11. X.H. Gao, X.N. Meng, L. Cui, and M.Y. Zhu: *Mater. Res. Express.*, 2019, vol. 6, 096583.
12. X.W. Zhang, C.F. Yang, and L.F. Zhang: *Metall. Res. Technol.*, 2020, vol. 117, pp. 110–21.
13. R. Diederichs and W. Bleck: *Steel Res. Int.*, 2016, vol. 77, pp. 202–09.
14. J.B. Xie, D.L. Hu, J.X. Fu, and H. Liu: *Ironmak. Steelmak.*, 2019, vol. 46, pp. 542–49.
15. Q.F. Shu, V.V. Visuri, T. Alatarvas, and T. Fabritius: *Metall. Mater. Trans. B*, 2020, vol. 51B, pp. 2905–16.
16. T.W. Clyne and W. Kurz: *Metall. Mater. Trans. A*, 1981, vol. 12A, pp. 965–71.
17. I. Ohnaka: *ISIJ Int.*, 1986, vol. 26, pp. 1045–51.
18. D. Tang, M. Ferreira, and P. Pistorius: *Microsc. Microanal.*, 2017, vol. 23, pp. 1082–90.
19. Y.M. Won and B.G. Thomas: *Metall. Mater. Trans. A*, 2001, vol. 32A, pp. 52–65.
20. J. Chen: *Manual of Chart and Data in Common Use of Steel Making*, 2nd ed. The Metallurgical Industry Press, Beijing, 2010, p. 510.
21. Z. Liu, J. Wei, and K. Cai: *ISIJ Int.*, 2007, vol. 42, pp. 958–63.
22. P. Wang, C.Z. Li, L. Wang, J.H. Zhang, and Z.L. Xue: *Metall. Mater. Trans. B*, 2021, vol. 52B, pp. 2056–71.
23. S.K. Choudhary and A. Ghosh: *ISIJ Int.*, 2009, vol. 49, pp. 1819–27.
24. M. Suzuki, R. Yamahuchi, K. Murakami, and M. Nakada: *ISIJ Int.*, 2001, vol. 41, pp. 247–56.
25. X.W. Zhang, L.F. Zhang, W. Yang, Y. Wang, and Y.Z. Li: *J. Iron Steel Res.*, 2007, vol. 29, pp. 724–31.
26. D. Tang and P.C. Pistorius: *Metall. Mater. Trans. B*, 2021, vol. 52B, pp. 51–58.

27. Z. Ma and D. Janke: *ISIJ Int.*, 1998, vol. 38, pp. 46–52.
28. R. Diederichs and W. Bleck: *Steel Res. Int.*, 2006, vol. 77, pp. 202–09.
29. H. Goto, K.I. Miyazawa, and H. Honma: *ISIJ Int.*, 2007, vol. 36, pp. 537–42.
30. X.M. Ding, Z. Liu, Q.L. Li, T.Y. Zhang, and C. Liu: *Arab. J. Sci. Eng.*, 2022, vol. 47, pp. 13857–72.

**Publisher's Note** Springer Nature remains neutral with regard to jurisdictional claims in published maps and institutional affiliations.

Springer Nature or its licensor (e.g. a society or other partner) holds exclusive rights to this article under a publishing agreement with the author(s) or other rightsholder(s); author self-archiving of the accepted manuscript version of this article is solely governed by the terms of such publishing agreement and applicable law.